

# Design of a Low Cogging Torque Axial Flux Multilayer Permanent Magnet Synchronous Machine for Wind Turbines Applications

Nabil Abdel-Karim\*, Semaan Georges\*\*, Mohamad Tarnini\*

\*Department of Electrical and Computer Engineering, Beirut Arab University, Debbieh Campus, Lebanon

\*\*Department of Electrical, Computer, and Communication Engineering, Notre Dame University, Lebanon

(n.abdelkarim@bau.edu.lb, sgeorges@ndu.edu.lb, m.tarnini@bau.edu.lb)

Received: 11.04.2018 Accepted: 11.06.2018

**Abstract-** For wind turbine generating systems, Axial Flux Permanent Magnet Synchronous Generators (AFPMSG) are becoming increasingly popular due to the many advantages they offer. Nevertheless, these machines suffer from the so-called cogging torque that affects the self-start ability and causes noise and mechanical vibration. Therefore, minimizing its effect is a major design concern for a reliable and smooth operation of small wind turbines. This paper presents a new method for reducing cogging torque based on stacking and shifting rotor magnets in the normal direction. First, the exact magnetic field distribution is computed using Maxwell's equations in magnetostatics. This analytical model takes into account the armature slotting effect and the multilayer permanent magnets configuration. Then, the cogging torque is computed by means of Maxwell's stress tensor. The accuracy of the proposed model is validated by FEA. Simulation results show that a substantial peak reduction can be achieved.

**Keywords** Axial flux machines, cogging torque, Maxwell's equations, wind energy systems.

## Nomenclature

	$ds, w_{s0}$	slot depth, slot opening
$A$		magnetic vector potential
$B_{RN(S)}^{(\ell)}$		Magnet remanence for the layer ' $\ell$ ' (North, South)
$B_{\phi}, B_z$		flux density components in $\phi z$ -coordinates
$C_k^{(v)}, D_k^{(v)}$		Fourier coefficients of the flux density in region ' $v$ '
$E_k^{(M,\ell)}, F_k^{(M,\ell)}$		Fourier coefficients of the remanence for a given layer ' $\ell$ '
$E_n^d, F_n^d$		Fourier coefficients of the winding distribution function
$f(k, n), g(k, n)$		auxiliary functions
$r_o, r_i, r_m$		outer, inner and mean radius
$\theta_{mN(S)}^{(\ell)}$		angular span of magnets for the layer ' $\ell$ ' (North, South)
$N_s, N_p$		Number of slots, number of poles

## 1. Introduction

Wind energy is clean, abundant and most of all renewable. Wind Turbine Generating Systems (WTGS) are used widely across the globe as part of modern power grids with a total installed capacity of 600-GW worldwide [1]. In 2017, 540-GW was installed compared to 487-GW in 2016 – a 11% increase. Being a main component of the worldwide electric energy markets [2], these systems can generate bulk energy using wind farms or they can be connected to the distribution systems as distributed generation units. A cost allocation model for scheduling smart grids based on the wind availability is given in [3]. Wind speed and direction can be analyzed using advanced statistical tools in order to predict the wind turbines energy output over a predefined time scale [4]. Off-shore wind farms with DC link are also attractive solutions for costal industrial loads, eliminating thus the need for the transmission system infrastructure [5]-[6]. Different types and topologies of electromechanical converters are used in these generating systems [7]-[8]. Among these, PMSGs gained special attention due to the benefits they provide such as direct coupling to the turbine shaft, elimination of the field winding and high power density. Nevertheless, this type of machines has an inherent structural handicap related to the cogging effect resulting from the magnetic interaction between the rotor magnets and the slotted armature. The cogging effect causes problems during start-up of wind turbines. At low cut-in wind speed (4-5m/s), the aerodynamic torque generated by the rotor blades should overcome the cogging torque or the turbine may not come out of stall and never start resulting thus in a loss of energy output [9]-[10]. Therefore, minimizing cogging torque for such applications is a decisive design parameter and reducing its undesirable effect will not only improve the performance of the synchronous generator but the performance of the whole generating system. The harmonics generated by the power converters can also hinder the operation of wind turbines and their elimination is a prime concern for designers [11]. For small wind turbine, it was reported that a cogging torque of 1N.m is good enough for a smooth self-start [12]-[13] and for permanent magnet direct-driven generators, its peak value should not exceed 2% of that of the net torque [14]. However, overall vibration in wind turbine systems is not only due to the cogging torque and it is also affected by the air resistance and the area of the blade in contact with the air [15]. Cogging torque reduction techniques have been extensively investigated in the literature. In [16], the optimal pole-arc-to-pole ratio is investigated. The effect of machine symmetry, magnet shifting, magnet skewing, and magnet shaping are analyzed in [17]-[20]. Skewing stator slots, tooth notching and slot

opening geometry are also efficient minimization techniques [21]-[22]. Moreover, magnet segmentation method and the use of non-overlapping concentrated winding have also proven to have a significant impact on controlling the cogging torque level [23]-[24]. Cogging torque requires the exact prediction of the airgap magnetic field distribution as affected by the slotted armature geometry. Traditionally, the field distribution can be calculated either by numerical or semi analytical methods. Numerical approaches require geometry discretization and meshing prior to the generation of the field solution. These modeling techniques offer many advantages such as handling nonlinear anisotropic materials but they require a great deal of computational time and resources. Therefore, a mesh-free solution is always preferred in the early design stage of electric machines. This paper describes the magnetic field distribution and the cogging torque calculation using Fourier analysis where the direct solution of Maxwell's equations in magnetostatics is considered. The cogging torque reduction technique is carried out by stacking and shifting the rotor magnets in the normal direction (Fig. 2). With this configuration, the cogging torque magnitude is greatly reduced to an acceptable level with little effect on the back-emf. Finally, FEA is applied in order to validate the analytical results and an excellent agreement is achieved. FEA is also a useful tool to carry out fatigue and stress analysis of wind turbines [25].

## 2. Model Formulation

The 3D geometry of an interior stator AFPMSG is shown in Fig.1. In this paper, the radial dependency of the magnetic field is neglected. This implies that the field solution is two-dimensional and it is carried out using polar coordinates. This is a valid assumption since the radial component will not greatly impact the magnetic field solution. Using FEA it was shown that the field radial component is zero at the

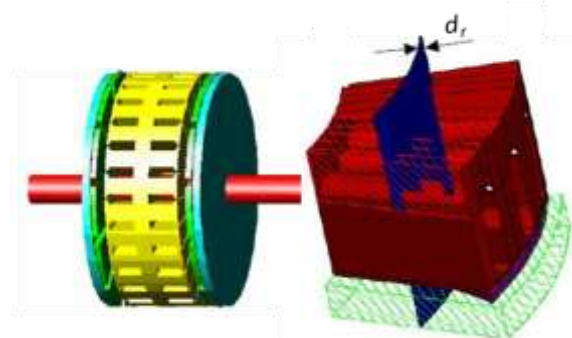


Figure 1. 3D geometry of the axial flux machine

machine's mean radius and gains some negligible amplitude as we move radially toward the machine's edges [26]. In order to improve the computation of the secondary parameters such as torque and back-emf, the machine is subdivided into  $N_{sl}$  radial annular slices and the magnetic vector potential solution is carried out for each slice  $d_r$ . The

different design parameters affecting the field solution are shown in fig (2). The rotor is equipped with multi-layer surface mounted permanent magnets. Layer one is made up of magnets 1 and 1' and so forth. In this study, each magnetic pole is composed of three magnet pieces shifted by an angle  $\theta_i^{(\ell)}$  and each layer ' $\ell$ ' is characterized by the magnets remanence  $B_{RN(S)}^{(\ell)}$ , their angular span  $\theta_{mN(S)}^{(\ell)}$ , and their relative angular position  $\theta_i^{(\ell)}$  with respect to the interpolar axis. All magnets are shifted by a given amount so that they all fit within a pole pitch. In order to obtain the 2D analytical solution, the following assumptions are made:

- the magnetic materials are linear, homogenous and infinitely permeable;
- the rotor magnets operates on the recoil line with a unity relative permeability and are magnetized in the normal direction;
- end effects are neglected and open armature slots with parallel sides are considered.

Since the magnetic materials are highly permeable, the magnetic field distribution is not calculated inside the soft-magnetic materials but Neumann conditions apply at their edges in order to predict the field distribution. To do so, the machine is divided into three regions, namely the current-carrying region (the slots), the source-free region (the airgap), and the magnetized region. For each region, Neumann boundary conditions, continuous boundary conditions or a combination of both are considered. Neumann conditions appear at the interfaces of the magnetic materials and the boundary conditions in the normal direction give rise to a set of linear algebraic system whose unknowns are the flux density coefficients.

### 3. Open-circuit Field Solution

The field solution is based on the magnetic potential vector  $\mathbf{A}$  which is a convenient way to find the flux density  $\mathbf{B}$  in each region of the machine. For magnetostatics problems, combining Maxwell's equations give rise to the well-known Poisson's equation:

$$\nabla^2 \mathbf{A} = -\mu \mathbf{J}_r - \nabla \times \mathbf{B}_{rem} \tag{1}$$

where  $\mathbf{J}_r$  and  $\mathbf{B}_{rem}$  are the current density vector and the remanence magnetization vector respectively. Written in polar coordinates Eq. (1) takes the following form:

$$\frac{1}{r_m^2} \frac{\partial^2 A_r}{\partial \varphi^2} + \frac{\partial^2 A_r}{\partial z^2} = -\left(\mu_0 J_r + \frac{1}{r_m} \frac{\partial B_R}{\partial \varphi}\right) \tag{2}$$

This partial differential form reduces to Laplace equation in the source-free region. Equation (2) has to be solved in different domains of the machine and this is done for each annular slice at the corresponding mean radius  $r_m$ . Moreover, since the cogging torque computation only requires the field produced by the magnets, the current density  $J_r$  is set to zero in Eq. (2). Since the flux density vector is given by  $\mathbf{B} = \nabla \times \mathbf{A}$ , the field components are related to the magnetic vector potential by:

$$B_\varphi = \frac{\partial A_r}{\partial z}; B_z = \frac{1}{r} \frac{\partial A_r}{\partial \varphi} \tag{3}$$

Using the separation of variables technique, the magnetic vector potential for a given region ' $v$ ' is given by:

$$A_r^{(v)} = a_0^{(v)} + \sum_{k \neq 0} \frac{r_m}{k\lambda} \left( C_k^{(v)} \operatorname{ch}\left(\frac{k\lambda z}{r_m}\right) + D_k^{(v)} \operatorname{sh}\left(\frac{k\lambda z}{r_m}\right) \right) \cdot \left( E_k^{(v)} \cos(k\lambda\varphi) + F_k^{(v)} \sin(k\lambda\varphi) \right) \tag{4}$$

where  $\lambda = \operatorname{gcd}(Ns, Np)$  and  $v = I, II$  and  $III$  is used for region indexing.  $Ns$  and  $Np$  denote the total number of slots and the number of magnet pole pairs respectively. For symmetric non-fractional slot machines,  $\lambda$  is usually equal to  $Np$ .

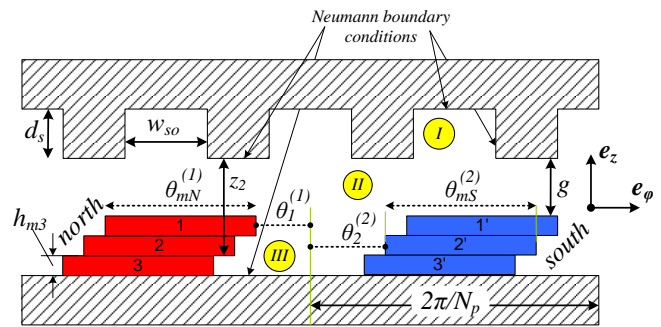


Figure 2. 2D cutaway of the machine at the mean radius

In the following subsections, field components are derived for each region by taking into account Neumann conditions and continuous boundary conditions at the interface of each domain.

#### 3.1 Slots area (region I)

This domain is made up of  $Ns/Np$  slots. For each slot, Neumann boundary conditions occur at the sides of the windable slot depth and at the bottom interface adjacent to the stator yoke. The Fourier expression of the field components in this region are:

$$B_\varphi^{(I,s)} = \sum_{m \neq 0} f_m^{(I,s)} \frac{\operatorname{sh}\left(\frac{m\pi(z+d_s)}{r_m w_{so}}\right)}{\operatorname{ch}\left(\frac{m\pi d_s}{r_m w_{so}}\right)} \cos\left(\frac{m\pi}{r_m w_{so}}(\varphi - \varphi_s)\right) \tag{5}$$

$$B_z^{(I,s)} = \sum_{m \neq 0} f_m^{(I,s)} \frac{\operatorname{ch}\left(\frac{m\pi(z+d_s)}{r_m w_{so}}\right)}{\operatorname{ch}\left(\frac{m\pi d_s}{r_m w_{so}}\right)} \sin\left(\frac{m\pi}{r_m w_{so}}(\varphi - \varphi_s)\right) \tag{6}$$

#### 3.2 Airgap field solution (region II)

In this source-free region, the tangential and normal components of the flux density are described respectively by Fourier series as:

$$B_\varphi^{(II)} =$$

$$\sum_{k \neq 0} \left( E_k^{(II)} \operatorname{sh}(kN_p z r_m^{-1}) + F_k^{(II)} \operatorname{ch}(kN_p z r_m^{-1}) \right) \sin(k\lambda\varphi) + \left( C_k^{(II)} \operatorname{sh}(kN_p z r_m^{-1}) + D_k^{(II)} \operatorname{ch}(kN_p z r_m^{-1}) \right) \cos(k\lambda\varphi) \quad (7)$$

$$B_z^{(II)} = \sum_{k \neq 0} \left( C_k^{(II)} \operatorname{ch}(kN_p z r_m^{-1}) + D_k^{(II)} \operatorname{sh}(kN_p z r_m^{-1}) \right) \sin(k\lambda\varphi) + \left( E_k^{(II)} \operatorname{ch}(kN_p z r_m^{-1}) + F_k^{(II)} \operatorname{sh}(kN_p z r_m^{-1}) \right) \cos(k\lambda\varphi) \quad (8)$$

The continuous boundary conditions for the airgap region and the top layer of the magnetized area are:

$$\begin{cases} B_{z|z=-g}^{(II)} = B_{z|z=-g}^{(III,1)} \\ B_{\varphi|z=-g}^{(II)} = B_{\varphi|z=-g}^{(III,1)} \end{cases} \quad (9)$$

The development of Eq. (9) gives the relation between the airgap field coefficients and those of the magnetized region as follows:

$$\begin{cases} C_k^{(II)} = C_k^{(III,1)} + F_k^{(M,1)} \operatorname{ch}(kN_p g r_m^{-1}) \\ D_k^{(II)} = D_k^{(III,1)} - F_k^{(M,1)} \operatorname{sh}(kN_p g r_m^{-1}) \\ E_k^{(II)} = E_k^{(III,1)} - E_k^{(M,1)} \operatorname{ch}(kN_p g r_m^{-1}) \\ F_k^{(II)} = F_k^{(III,1)} + E_k^{(M,1)} \operatorname{sh}(kN_p g r_m^{-1}) \end{cases} \quad (10)$$

Subscript 'III, i' refers to the layer 'i' in the magnetized region III. These coefficients are obtained by applying the boundary conditions in the normal direction between the different regions.

### 3.3 Permanent magnets domain (region III)

It is assumed that the magnets are normally magnetized and are invariant in the normal direction. The remanence function is written as:

$$B_R^{(\ell)}(\varphi) = \sum_{k \neq 0} E_k^{(M,\ell)} \cos(kN_p \varphi) + F_k^{(M,\ell)} \sin(kN_p \varphi) \quad (11)$$

The  $n^{\text{th}}$  harmonic Fourier coefficients in (11) for a given layer ' $\ell$ ' are given by:

$$E_k^{(M,\ell)} = \frac{-1^{(k)}}{k\pi} \left\{ \begin{aligned} & B_{RN}^{(\ell)} (\sin kN_p (\theta_1^{(\ell)} + \theta_{mN}^{(\ell)} - \theta_0) - \sin kN_p (\theta_1^{(\ell)} - \theta_0)) \\ & B_{RS}^{(\ell)} (\sin kN_p (\theta_2^{(\ell)} + \theta_{mS}^{(\ell)} + \theta_0) - \sin kN_p (\theta_2^{(\ell)} + \theta_0)) \end{aligned} \right. \quad (12)$$

$$F_k^{(M,\ell)} = \frac{-1^{(k)}}{k\pi} \left\{ \begin{aligned} & B_{RN}^{(\ell)} (\cos kN_p (\theta_1^{(\ell)} + \theta_{mN}^{(\ell)} - \theta_0) - \cos kN_p (\theta_1^{(\ell)} - \theta_0)) \\ & B_{RS}^{(\ell)} (\cos kN_p (\theta_2^{(\ell)} + \theta_{mS}^{(\ell)} + \theta_0) - \cos kN_p (\theta_2^{(\ell)} + \theta_0)) \end{aligned} \right. \quad (13)$$

$B_{RN}^{(\ell)}$  and  $B_{RS}^{(\ell)}$  are the north and south induction remanence for a given layer ' $\ell$ ' and  $\theta_0$  denotes the angle of rotation. Knowing that the source terms are expressed as Fourier series, then each term creates like harmonic term in the flux density expression and the expression of the field components becomes:

$$B_{\varphi}^{(III,i)} =$$

$$\sum_{k \neq 0} \left( E_k^{(III,i)} \operatorname{sh}(kN_p z r_m^{-1}) + F_k^{(III,i)} \operatorname{ch}(kN_p z r_m^{-1}) \right) \sin(kN_p \varphi) + \left( C_k^{(III,i)} \operatorname{sh}(kN_p z r_m^{-1}) + D_k^{(III,i)} \operatorname{ch}(kN_p z r_m^{-1}) \right) \cos(kN_p \varphi) \quad (14)$$

$$B_z^{(III,i)} = \sum_{k \neq 0} \left( C_k^{(III,i)} \operatorname{ch} \frac{kN_p z}{r_m} + D_k^{(III,i)} \operatorname{sh} \frac{kN_p z}{r_m} + F_k^{(M,i)} \right) \sin(kN_p \varphi) + \left( E_k^{(III,i)} \operatorname{ch} \frac{kN_p z}{r_m} + F_k^{(III,i)} \operatorname{sh} \frac{kN_p z}{r_m} - E_k^{(M,i)} \right) \cos(kN_p \varphi) \quad (15)$$

For this region, Neumann boundary conditions in the normal direction are satisfied at the rotor yoke surface leading to:

$$\begin{cases} D_k^{(III,3)} = -C_k^{(III,3)} T_{kN_p}(z_3) \\ F_k^{(III,3)} = -E_k^{(III,3)} T_{kN_p}(z_3) \end{cases} \quad (16)$$

Equations (15) in (16) give:

$$B_{\varphi}^{(III,3)} = \sum_{k \neq 0} \left( E_k^{(III,3)} \sin(kN_p \varphi) + C_k^{(III,3)} \cos(kN_p \varphi) \right) \cdot \left( \operatorname{sh}(kN_p z r_m^{-1}) - T_{k\lambda}(z_3) \operatorname{ch}(kN_p z r_m^{-1}) \right) \quad (17)$$

$$B_z^{(III,3)} = \sum_{k \neq 0} \left( C_k^{(III,3)} \left( \operatorname{ch} \frac{kN_p z}{r_m} - T_{kN_p z_3} \frac{kN_p z}{r_m} \right) + F_k^{(M,i)} \right) \sin(kN_p \varphi) + \left( E_k^{(III,3)} \left( \operatorname{ch} \frac{kN_p z}{r_m} - T_{k\lambda z_3} \operatorname{sh} \frac{kN_p z}{r_m} \right) - E_k^{(M,i)} \right) \cos(kN_p \varphi) \quad (18)$$

Moreover, the boundary conditions between different layers of the magnetized region lead to the following set of equations describing the relationship between the field coefficients of the different layers as follows:

$$\begin{cases} C_k^{(III,1)} = C_k^{(III,3)} + \sum_{i=1}^{N_{\ell}-1} (F_k^{(M,i+1)} - F_k^{(M,i)}) \operatorname{ch}(kN_p z_i r_m^{-1}) \\ D_k^{(III,1)} = D_k^{(III,3)} + \sum_{i=1}^{N_{\ell}-1} (F_k^{(M,i)} - F_k^{(M,i+1)}) \operatorname{sh}(kN_p z_i r_m^{-1}) \\ E_k^{(III,1)} = E_k^{(III,3)} + \sum_{i=1}^{N_{\ell}-1} (E_k^{(M,i)} - E_k^{(M,i+1)}) \operatorname{ch}(kN_p z_i r_m^{-1}) \\ F_k^{(III,1)} = F_k^{(III,3)} + \sum_{i=1}^{N_{\ell}-1} (E_k^{(M,i+1)} - E_k^{(M,i)}) \operatorname{sh}(kN_p z_i r_m^{-1}) \end{cases} \quad (19)$$

and

$$\begin{cases} C_k^{(III,2)} = C_k^{(III,3)} + (F_k^{(M,3)} - F_k^{(M,2)}) \operatorname{ch}(kN_p z_2 r_m^{-1}) \\ D_k^{(III,2)} = D_k^{(III,3)} + (F_k^{(M,2)} - F_k^{(M,3)}) \operatorname{sh}(kN_p z_2 r_m^{-1}) \\ E_k^{(III,2)} = E_k^{(III,3)} + (E_k^{(M,2)} - E_k^{(M,3)}) \operatorname{ch}(kN_p z_2 r_m^{-1}) \\ F_k^{(III,2)} = F_k^{(III,3)} + (E_k^{(M,3)} - E_k^{(M,2)}) \operatorname{sh}(kN_p z_2 r_m^{-1}) \end{cases} \quad (20)$$

In these equations,  $Z_{i(=1,2,3)}$  is the distance in the normal direction measured between the interface of the airgap/teeth and the bottom of the magnet that belongs to the layer ' $\ell$ ' as

depicted in fig (2). It is important to note at this point that if aligned magnets are considered (without any shifting), the coefficients  $E_k^{(M,1)}$ ,  $E_k^{(M,2)}$  and  $E_k^{(M,3)}$  are all identical and  $E_k^{(III,1)} = E_k^{(III,2)} = E_k^{(III,3)}$ . This is the case of rotors with single magnetic poles (all magnets are aligned).

### 3.4 Derivation of Fourier coefficients for the Magnetized region

A combination of Neumann and boundary conditions occurs at the interface between region I and region II. The boundary conditions apply between the airgap and the slot openings. For a given slot 's' ( $\varphi_s \leq \varphi \leq \varphi_s + w_s$ ):

$$\begin{cases} B_{z|z=0}^{(s)} = B_{z|z=0}^{(II)} \\ B_{\varphi|z=0}^{(s)} = B_{\varphi|z=0}^{(II)} \end{cases} \quad (21)$$

Additional boundary conditions between the airgap and the magnetic regions adjacent to it ( $\varphi_s + w_s \leq \varphi \leq \varphi_{s+1}$ ) are

$$B_{\varphi|z=0}^{(s)} = 0 \quad (22)$$

The following system of linear equations follows from the application of eq. (21) and (22).

$$\begin{aligned} T_{k\lambda}(z_3)C_k^{(III,3)} + \sum_{n \neq 0} (g(k,n) - f(k,n))C_n^{(III,3)} = \\ -F_k^{(M,1)}S_{k,01} - F_k^{(M,2)}S_{k,12} - F_k^{(M,3)}S_{k,20} \\ - \sum_{n \neq 0} \left( F_n^{(M,1)}C_{n,01} + F_n^{(M,2)}C_{n,12} + F_n^{(M,3)}C_{n,2\frac{j\pi}{2}} \right) \\ (g(k,n) - f(k,n)) \end{aligned} \quad (23)$$

$$\begin{aligned} T_{k\lambda}(z_3)E_k^{(III,3)} + \sum_{n \neq 0} (g(k,n) + f(k,n))E_n^{(III,3)} = \\ E_k^{(M,1)}S_{k,01} + E_k^{(M,2)}S_{k,12} + E_k^{(M,3)}S_{k,20} \\ + \sum_{n \neq 0} \left( E_n^{(M,1)}C_{n,01} + E_n^{(M,2)}C_{n,12} + E_n^{(M,3)}C_{n,2\frac{j\pi}{2}} \right) \\ (g(k,n) + f(k,n)) \end{aligned} \quad (24)$$

The auxiliary functions  $C_k$  and  $S_k$  are defined as follows:

$$\begin{aligned} S_{k,ab} &= \text{sh}(kN_p z_a / r_m) - \text{sh}(kN_p z_b / r_m) \\ C_{k,ab} &= \text{ch}(kN_p z_a / r_m) - \text{ch}(kN_p z_b / r_m) \end{aligned}$$

Functions  $f$  and  $g$  are only defined when  $k \pm n$  are multiple of  $N_s/N_p$  giving rise to large sparse matrices represented by sparse data structures proportional to the nonzero entries. Their corresponding expressions are found in appendix A. With sparse programming, computing higher harmonic orders for the magnetic field is possible without leading to ill-conditioned matrices. For the airgap magnetic field computation, considering the first 128 harmonics usually gives satisfactory results. In this context, sparsity techniques in MATLAB were used and substantial savings in terms of both computational time and resources have been made. The sparse matrix form for eq. (23) and (24) is:

$$C_k^{(III,3)} = -(T_{\lambda p, z_3} \mathbf{H})^{-1} \begin{bmatrix} (S_{k,01} + C_{k,01} \mathbf{H}) \mathbf{F}_k^{(M,1)} + \\ (S_{k,12} + C_{k,12} \mathbf{H}) \mathbf{F}_k^{(M,2)} + \\ (S_{k,20} + C_{k,2\frac{j\pi}{2}} \mathbf{H}) \mathbf{F}_k^{(M,3)} \end{bmatrix} \quad (25)$$

and

$$E_k^{(III,3)} = (T_{\lambda p, z_3} \mathbf{L})^{-1} \begin{bmatrix} (S_{k,01} + C_{k,01} \mathbf{L}) \mathbf{E}_k^{(M,1)} + \\ (S_{k,12} + C_{k,12} \mathbf{L}) \mathbf{E}_k^{(M,2)} + \\ (S_{k,20} + C_{k,2\frac{j\pi}{2}} \mathbf{L}) \mathbf{E}_k^{(M,3)} \end{bmatrix} \quad (26)$$

$S$  and  $T$  are diagonal matrices of order  $k$ ,  $C$  is a square matrix made up of identical rows,  $\mathbf{H}(\mathbf{i}, \mathbf{j}) = \mathbf{g}(\mathbf{i}, \mathbf{j}) - \mathbf{f}(\mathbf{i}, \mathbf{j})$  and  $\mathbf{L}(\mathbf{i}, \mathbf{j}) = \mathbf{g}(\mathbf{i}, \mathbf{j}) + \mathbf{f}(\mathbf{i}, \mathbf{j})$ . Equations (25) and (26) results in the exact solution of the magnetic field coefficients in the sub-region (III, 3) described by eq. (17) and (18).

## 4. Cogging Torque Expression

Torque computation is performed using Maxwell stress tensor method applied at the interface region between the airgap and the PM magnets. The elementary force acting on one disc is given by  $d\mathbf{F} = \sigma_n ds + \sigma_t ds$ . While the first component acts on the normal direction and can twist the discs, the second one is responsible for the torque production expressed in the following integral form:

$$\begin{aligned} \Gamma &= \iint_{(Ag)} r \mathbf{e}_r \times d\mathbf{F} = \iint_{(Ag)} (\mu_0 H_n H_t) r^2 dr d\varphi \mathbf{e}_z \\ &= \mu_0^{-1} \int_0^{2\pi} \int_{r_i}^{r_o} B_{\varphi|z=-g}^{(III,1)} B_{z|z=-g}^{(III,1)} d\varphi \mathbf{e}_z \end{aligned} \quad (27)$$

Inserting the equations derived previously for the field solution and developing, the magnitude of the cogging torque is expressed by:

$$\begin{aligned} \Gamma_{cog} &= \pi(3\mu_0)^{-1} \sum_{s=1}^{N_{sl}} (R_{o,s}^3 - R_{i,s}^3) \\ &\times \sum_{n \neq 0} (C_{n,s}^{(III,1)} E_n^{(M,1)} + E_{n,s}^{(III,1)} F_n^{(M,1)}) \cdot \\ &\quad \times (sh(nz_0) - T_{n\lambda}(z_1)ch(nz_0)) \end{aligned} \quad (28)$$

For disc-type machines, representing the machine by ten radial slices is considered a good practice for predicting the global quantities with an acceptable accuracy.

## 5. Induced Voltage Calculation

The magnetic flux produced by the magnets linking a pole pair for phase 'm' is given by:

$$\phi_g = \int_0^{\frac{2\pi}{N_p}} \int_{r_i}^{r_o} F_{d,m}(\varphi) B_{z|z=0}^{(II)} r dr d\varphi \quad (29)$$

The winding distribution function  $F_{d,m}$  depicted in Fig. (3) carries information about the winding topology such as slot opening, coil span and location [27]. The corresponding Fourier series is expressed by:

$$F_{d,m}(\varphi) = a_0 + \sum_{n \neq 0} E_n^d \cos n \left( N_p \varphi - \frac{2(m-1)k\pi}{3} \right) + F_n^d \sin n \left( N_p \varphi - \frac{2(m-1)k\pi}{3} \right) \quad (30)$$

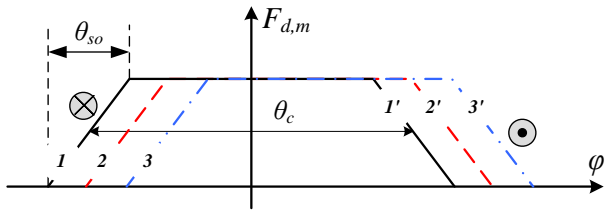


**Figure 3.** Illustration of a coil group distribution function

The total flux per phase produced by the magnets is obtained by adding each elementary flux of all series-connected coils. Substituting (30) in (29) and developing:

$$\phi_{g,m} = \pi(r_o^2 - r_i^2)/2 \times \sum_{k \neq 0} a_k^{(II)} \left( E_n^d \sin \frac{2(m-1)k\pi}{3} + F_n^d \cos \frac{2(m-1)k\pi}{3} \right) + \sum_{k \neq 0} b_k^{(II)} \left( F_n^d \sin \frac{2(m-1)k\pi}{3} - E_n^d \cos \frac{2(m-1)k\pi}{3} \right) \quad (31)$$

$r_o$  and  $r_i$  are the outer radius and the inner radius of a given annular slice respectively. The back emf requires the flux calculation at the stator surface, i.e.  $z = 0$ . Moreover, if the axis of the coil is taken as reference, only the cosine terms in (30) exist and the flux expression is then reduced to:

$$\phi_{g,m} = \pi(r_o^2 - r_i^2)/2 \times \sum_{k \neq 0} E_k^d \left( C_k^{(II)} \sin \frac{2(m-1)k\pi}{3} - E_k^{(II)} \cos \frac{2(m-1)k\pi}{3} \right) \quad (32)$$

The winding pitch factor and the slot opening factor are considered in the expression of the coefficient  $E_n^d$  [28]. The back emf for phase 'a' at a given rotational speed  $\Omega$  is obtained by differentiating (32) with respect to time, i.e.

$$e_{ph} = -d\phi/dt = -\Omega d\phi/d\theta \quad (33)$$

and developing, we get:

$$e_{ph} = -\Omega \pi (r_o^2 - r_i^2) \times \sum_{k \neq 0} E_k^d \frac{d}{d\theta} \left( E_k^{(III,1)} - E_k^{(M,1)} ch(kN_p g r_m^{-1}) \right) \quad (34)$$

The differentiation of the different coefficients with respect to the angular position is shown in appendix B.

### 6. Validation of the Analytical Model

In order to validate the proposed analytical model, the airgap flux density and the global parameters are checked using FEM. The FEM analysis is performed for the 2D configuration at the machine's mean radius as depicted in Fig. (4) under no-load conditions. The geometric dimensions and magnetic specifications of the simulated generator are given in table 1 in the appendix B.

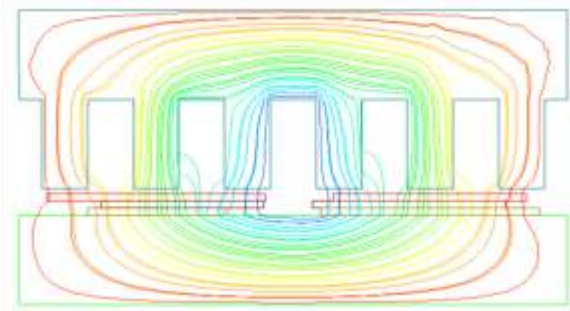


**Figure 4.** Illustration of the flux lines in different parts of the generator

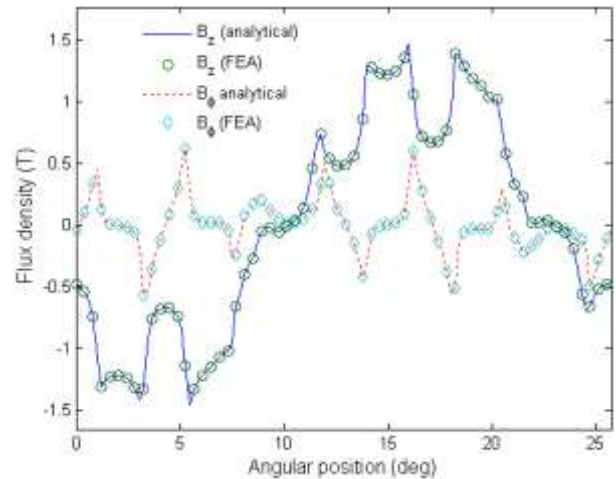


**Figure 5.** Airgap flux density distribution

A comparison of the predicted airgap flux density distribution calculated by the analytical approach and the FEM is shown in Fig. (5). As can be seen, there is a good correlation between the two models. This matching of results is also a good indicator that both back-emf and cogging torque can also be predicted with a great accuracy using the proposed analytical approach.

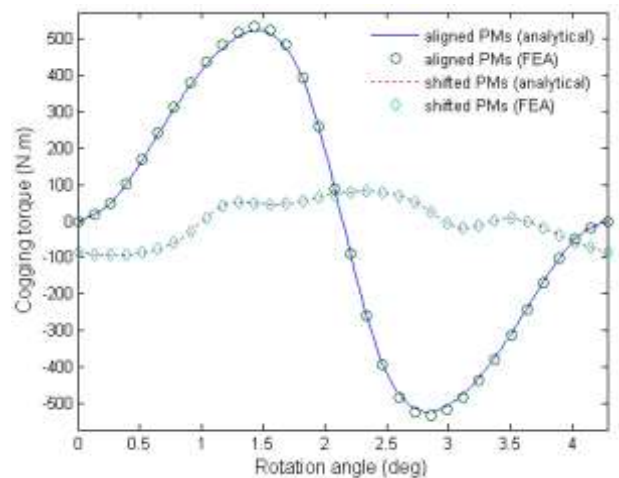


**Figure 6.** Cogging torque as affected by magnet shifting

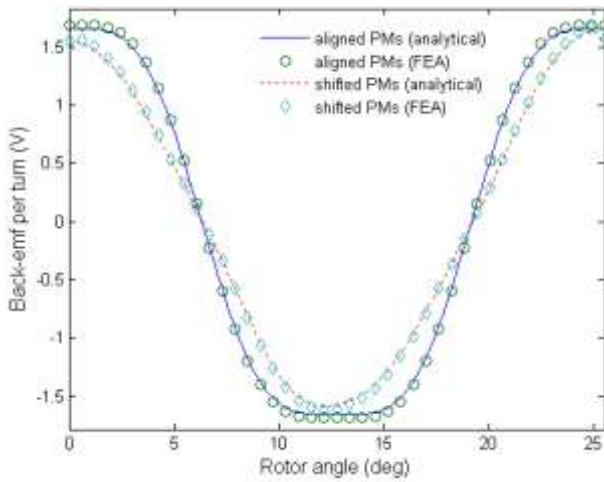


Figure 7. Back-emf waveforms at 230rpm

Figure (6) shows the waveform of the cogging torque for both cases: aligned magnets and shifted magnets while the back-emf curves for a 10-kW machine are depicted in Fig. (7). As expected, the analytical prediction fairly agrees with the finite element solution.

In this design technique, PMs of 2mm thickness are considered which could lead to some manufacturing imperfection in terms of geometric dimensions, positioning/eccentricity, and magnetization precision. According to [29], rotor eccentricity can affect the cogging torque and no major start-up problem occurs up to 33% dynamic eccentricity.

7. Conclusion

A quasi-2D analytical model formulated in polar coordinates based on Maxwell’s equations has been derived for a multilayer surface mounted permanent magnet generator where each magnet is subdivided into three pieces shifted in the normal direction. This approach is applicable for both internal and external machines and requires by far less computational time and resources than the FEM. The magnetic field distribution, the cogging torque, and the back-emf waveforms all show an excellent agreement with those obtained from FEA. Simulation results show that stacking and shifting magnets in the normal direction will not only reduce the cogging torque to a low level but also improves the back-emf waveform without any considerable loss of magnitude. Therefore, it is suitable during the initial pre-design stage of wind turbines generating systems where the cogging torque is a major start-up concern at low wind speed.

APPENDIX A

Functions *f* and *g* relevant to the calculation of the magnetic field distribution are given by:

$$f(k, n) = \sum_{m \neq 0} \frac{(2mkN_s N_p w_{so}^2) T_{m\pi} \left(\frac{d_s}{r_m}\right) \delta_m \left(\frac{-n}{2} N_p w_{so}, \frac{k}{2} N_p w_{so}\right)}{\left((m\pi)^2 - (kN_p w_{so})^2\right) \left((m\pi)^2 - (nN_p w_{so})^2\right)}$$

$$g(k, n) =$$

$$\sum_{m \neq 0} \frac{(2mkN_s N_p w_{so}^2) T_{m\pi} \left(\frac{d_s}{r_m}\right) \delta_m \left(\frac{n}{2} N_p w_{so}, \frac{k}{2} N_p w_{so}\right)}{\left((m\pi)^2 - (kN_p w_{so})^2\right) \left((m\pi)^2 - (nN_p w_{so})^2\right)}$$

The  $\delta$ -function is defined by:

$$\delta_m(a, b) = \begin{cases} 2 \cos(a) \cos(b) & m \text{ odd} \\ -2 \sin(a) \sin(b) & m \text{ even} \end{cases}$$

APPENDIX B

The differentiation of the field coefficients with respect to the angular position for the back emf computation is carried out by solving the linear system:

$$\frac{dE_k^{(M,3)}}{d\theta} = (T_{\lambda p}(z_3)L)^{-1} \begin{bmatrix} (S_{k,01} + C_{k,01}L) \frac{dE_k^{(M,1)}}{d\theta} + \\ (S_{k,12} + C_{k,12}L) \frac{dE_k^{(M,2)}}{d\theta} + \\ (S_{k,20} + C_{k,2\frac{j\pi}{2}}L) \frac{dE_k^{(M,3)}}{d\theta} \end{bmatrix}$$

where

$$\frac{dE_k^{(M,\ell)}}{d\theta} = \frac{-(-1)^{(k)} \left\{ \begin{aligned} &B_{RN}^{(\ell)} \left( \cos kN_p \left( \theta_1^{(\ell)} + \theta_{mN}^{(\ell)} - \theta_0 \right) - \cos kN_p \left( \theta_1^{(\ell)} - \theta_0 \right) \right) \\ &+ \\ &B_{RS}^{(\ell)} \left( \cos kN_p \left( \theta_2^{(\ell)} + \theta_{mS}^{(\ell)} + \theta_0 \right) - \cos kN_p \left( \theta_2^{(\ell)} + \theta_0 \right) \right) \end{aligned} \right\}}{k\pi}$$

Table 1. Parameters of the simulated machine

number of slots	84	magnet fraction, north (%)	70, 60, 50
pole pairs	14	magnet fraction, south (%)	70, 70, 60
magnetization	parallel	magnet spacing, north (%)	50, 25, 50
outer radius (mm)	35	magnet spacing, south (%)	50, 25, 50
inner radius (mm)	30		
airgap length (mm)	1.5		
slot fraction (%)	50		
PMs thickness (mm)	2/piece		

References

- [1] Renewable energy policy framework for the 21<sup>st</sup> century, REN21, <http://www.ren21.net>.
- [2] G. Longoria, D. Jiang and A. Davy, “Wind energy allocation strategies for long-term contracts in open energy markets”, International Conf. on renewable energy research and applications (ICRERA), 2016.
- [3] S. Konda, L. Panwar, S. Goutham, , “A dynamic penalty cost allocation based uncertain wind energy scheduling in smart grids”, Int. Journal of Renewable Energy Research (IJRER), Vol.7, 2017.
- [4] U. Mohankumar, M. Athul and J. Freeman, “Remote triggered monitoring of wind performance using Weibull and Rayleigh distributions,” International Conf. on renewable energy research and applications (ICRERA), 2017.
- [5] N. Kimura, “Offshore wind energy with HVDC link transmission: recent development in Japan,” International Conf. on Advances in Power System Control, Operation & Management, 2017.
- [6] S. Chaithanya, V. Reddy, R. Kiranmayi, “A state of art review on offshore wind power transmission using low frequency AC system”, Int. Journal of Renewable Energy Research (IJRER), Vol.8, 2018.

- [7] A. Beainy, C. Maatouk, and N. Moubayed, "Comparison of different types of generator for wind energy conversion system topologies", *Renewable Energy for Developed Countries REDEC*, 2016.
- [8] S. Mishra, A. Kumar, "Application of brushless excitation system in wind power generation", *International Conf. on renewable energy research and applications (ICRERA)*, 2015.
- [9] A. Kumari, S. Marwaha and A. Marwaha, "Comparison of methods of minimization of cogging torque in wind generators using FE analysis," *Journal of the Indian Institute of Science*, 2006, 86, pp. 355–362.
- [10] N. Min-Fu and Y. Yu-Han, "Rotor eccentricity effect on cogging torque of PM generators for small wind turbines," *IEEE transaction on Magnetics*, 2013, 49, (5), pp. 1897–1900.
- [11] M. Ferrari, "GSC control strategy for harmonic voltage elimination of grid-connected DFIG wind turbine", *International Conf. on renewable energy research and applications (ICRERA)*, 2014.
- [12] E. Muljadi and J. Green, "Cogging torque reduction in a permanent magnet wind turbine generator," in *Proceedings of 21st American Society of Mechanical Engineers Wind Energy Symposium*, Nevada, January 2002.
- [13] M. Lukaniszyn and A. Mlot, "Analysis of a BLDC motor with fractional slot winding," in *Proceedings of Electrotechnical Institute, Technical University of Opole*, vol. 229, pp. 115–125, 2006.
- [14] J. Sapanen, V. Ruuskanen, V., Nerg and J. Pyrhönen, "Dynamic torque analysis of a wind turbine drive train including a direct-driven permanent-magnet generator," *IEEE Transaction on Industrial Electronics*, vol. 58, pp. 3859–3867, 2011.
- [15] K. Abdulraheem, G. Al-Kindi, "Wind turbine condition monitoring using multi-sensor data system," *Int. Journal of Renewable Energy Research (IJRER)*, Vol.8, 2018.
- [16] H. Qingling and W. Qunjing, "Design techniques for reducing cogging torque in low-speed permanent magnet wind power generator," *Int. Conf. on Electrical Machines and Systems (ICEMS)*, Beijing, China, pp. 1–3, 2011.
- [17] M. Gulec and M. Aydin, "Magnet asymmetry in reduction of cogging torque for integer slot axial flux permanent magnet motors," *IET Electric Power Applications*, vol. 8, pp. 189–198, 2014.
- [18] M. Bendib, M. Hachemi, F. Marignetti, "Electromagnetic Design and Analysis of a Novel Axial-Transverse Flux Permanent Magnet Synchronous Machine," *Electric Power Components and Systems*, vol.45, pp912-924, 2017.
- [19] S. Zhu, Z. Jiang, Z. Zhu and C. C. Chan, "Analytical methods for minimizing cogging torque in permanent-magnet machines," *IEEE Transactions on Magnetics*, vol. 45, pp. 2023–2031, 2009.
- [20] V. Sempere, M.B. Payán, and J.C. Bueno, "Cogging Torque Cancellation by Magnet Shaping in surface mounted permanent magnet motors," *IEEE Transactions on Magnetics*, vol. 53, no. 7, 2017.
- [21] Y. Ueda, H. Takahashi, A. Ogawa, T. Akiba and M. Yoshida, "Cogging-Torque Reduction of Transverse-Flux Motor by Skewing Stator Poles", *IEEE Transactions on Magnetics*, vol. 52, 2016.
- [22] W. Ren and Q. Xu, "A novel technique of cogging torque reduction in mass-produced surface mounted permanent magnet motor using tooth notching pairing", *IEEE International Magnetics Conference*, July 2015.
- [23] A. Ghasemi, "Cogging-Torque reduction and optimization in surface mounted permanent magnet motor using magnet segmentation method", *Electric Power Components and Systems*, vol.42, pp1239-1278, 2014.
- [24] N. Levin, V. Pugachov and S. Orlova, "Direct-drive contactless wind generator with concentrated winding", *Latvian Journal of Physics and Technical Sciences*, vol. 49, pp. 14–20, 2012.
- [25] A. Pehlivan, M. Aksit, "Fatigue analysis approach of a 500-kW wind turbine main load frame", *International Conf. on renewable energy research and applications (ICRERA)*, 2013.
- [26] H. Tiegna, A. Bellara, Y. Amara, and G. Barakat, "Analytical modeling of the open-circuit magnetic field in axial flux permanent-magnet machines with semi-closed slots", *IEEE Transactions on Magnetics*, vol. 48, pp.1212-1226, 2012.
- [27] V. Ostovic, "Dynamics of saturated electric machines", *Springer-Verlag*, 1989.
- [28] N. Abdel-Karim, J. Azzouzi and G. Barakat, "Winding function theory and Maxwell's equations coupled analytical modeling of an axial flux PM synchronous machine", *International Revue of Electrical Engineering*, vol. 0, 2006.
- [29] Min-Fu Hsieh, Yu-Han Yeh, "Rotor Eccentricity Effect on Cogging Torque of PM Generators for Small Wind Turbines", *IEEE Transactions on Magnetics*, vol. 49, pp. 1897–1900, 2013.